ME6103 Final Project, Spring 2025

Dakota Dyer, James Hamilton,

Nina Latorre, Shubh Raval

Optimization of a Spherical Parallel Manipulator for Enhanced Performance in Human-Centric Environments

Introduction

With the increasing adoption of collaborative robots (cobots) in automating complex manual tasks, there is a growing demand for wrist mechanisms that are precise, efficient, lightweight, and capable of delivering dexterous rotational motion across a wide range of applications. Typical robotic arms employ three serially connected rotary (3R) joints to achieve wrist articulation or use a differential wrist drive. However, these configurations suffer from several limitations, including high inertia, reduced precision, kinematic constraints, and a less compact design. In particular, robotic arms attempting dexterous reorientation about a fixed point creates major difficulty to reach joint poses that are feasible or do not require massive repositioning of the entire arm. Additionally, at the edges of a robotic arm's reach, they face a high density of positions and orientations which cause the robot to lose degrees of freedom often called singularities. In these edges of the workspace, reorientation about a fixed point can be impossible for typical robotic arms. With growing applications in human centric environments with complex object manipulation tasks, this is a challenge that will need to be surmounted.

A Spherical Parallel Manipulator (SPM) offers a promising alternative or addition to serial 3 rotational axis wrist mechanisms by providing three rotational degrees of freedom in a parallel, structurally rigid configuration. With actuators located at the base, the SPM benefits from reduced inertia and improved dynamic response. Additionally, the load path through passive links enables the use of smaller, lower-power actuators while still maintaining effective end-effector control. Despite these advantages, SPMs have not been widely adopted as wrist mechanisms due to limited research, especially in the context of collaborative robotics, and the complexity of their kinematic modeling.

In this study, we aim to optimize an SPM design inspired by the human wrist for cobot applications. Specifically, we seek to maximize the manipulator's range of motion while minimizing its total mass, using design targets derived from human wrist performance. We will use multi-objective optimization methods such as Design of Experiments (DoE), the NSGA-II genetic algorithm, design space exploration methods, and model validation techniques, to explore and arrive at optimal critical parameters for a SPM design.
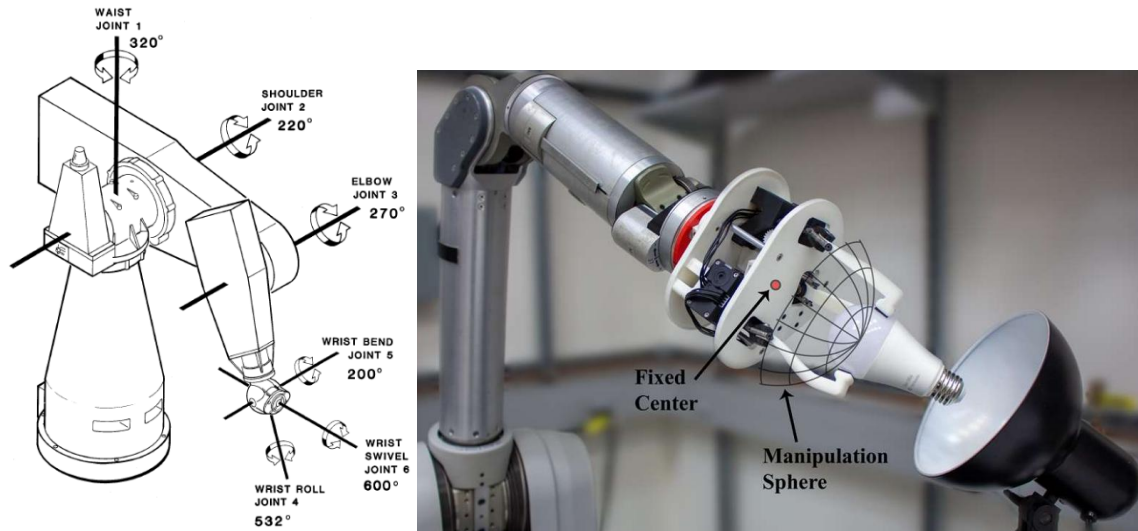

Figure 1: Programmable Universal Manipulation Arm (PUMA) with a three rotational axis (3R) wrist verus a 6 DOF robot with a SPM attachment ([ref](#)).

Point of Reference

Optimization for this mechanism will use the average, relevant parameters of a human wrist as a point of reference for performance evaluation of the SPM. Functionally, this would be related to the human wrist's geometric configuration is reflected in the kinematic assessment of the wrist. This framework facilitates the development of optimal solutions of the SPM for complex, manual tasks. Key aspects of a wrist for manipulation are wrist rotation range and physical size.

Human wrist parameters will serve as the point of reference and will influence how the objective functions are constrained
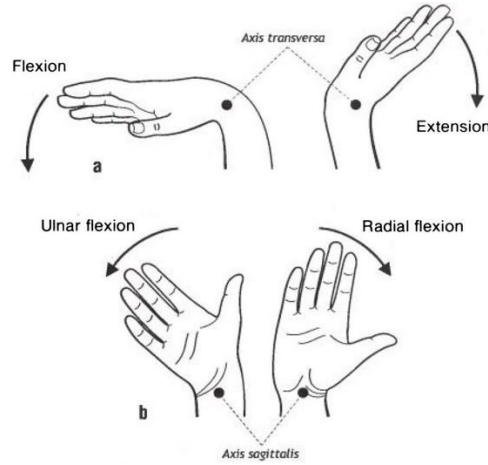
Figure 2: Movements on the human wrist

Figure 2 demonstrates the range of motion our system aims to exceed; given that the average human wrist's rotation along the Sagittal axis is less than that of the Transverse axis, a goal range of motion would be achieving an average rotation angle across both axes. The system will aim to approach or minimize relative too, the average size of a human wrist relating to diameter and height. Table 1 below depicts the average capabilities of a human hand with which gives our system a point of reference.

Table 1: Average Human Wrist Motion & Geometric Parameters

Parameter	Value
Avg Wrist Rotation (°)	48°-55° [1]
Avg Wrist Diameter (mm)	52.52 [5]
Avg Metacarpal Length Range (mm)	~45-75 [9]

Optimization Goals

With a reference framework in place, we now define the optimization goals. One of the primary functional requirements for the SPM is the ability to support a payload with minimal deflection. Since this wrist mechanism is intended to be integrated with other end-effector components (e.g., grippers or tools), it must accommodate both the payload and the forces generated during task execution. Within this scope, we aim to ensure

consistent load support throughout the defined workspace. A representative load case will define the nominal load and torque values that must be satisfied by the design, with safety factors used to generalize performance across edge cases.

We aim to minimize the form factor and mass of the SPM to improve the effective payload capacity of the overall robotic system. A smaller volume footprint reduces collision risk during complex manipulations, while lower mass decreases the load burden on upstream joints. To assess the kinematic performance of the manipulator, we chose to use a quality metric called the Global Conditioning Index (GCI) as an objective function. The global condition defines how well a particular manipulator can move through its workspace without reaching singularities. While GCI does not quantify the absolute geometric limits of the mechanism's motion, it serves as an effective surrogate by evaluating the condition number of the Jacobian matrix, which relates joint velocity to cartesian velocity across different orientations. A high GCI value implies more uniform and dexterous motion capabilities, which is a key performance trait for wrist mechanisms. Rather than attempting to compare manipulators orientation by orientation and assess their performance, the GCI is a single number index to compare manipulators against each other based on if their workspace conditioning is closer to 0 (poor) or 1 (ideal). This approach enables consistent evaluation across design iterations without sacrificing meaningful insight into the system's kinematic performance.
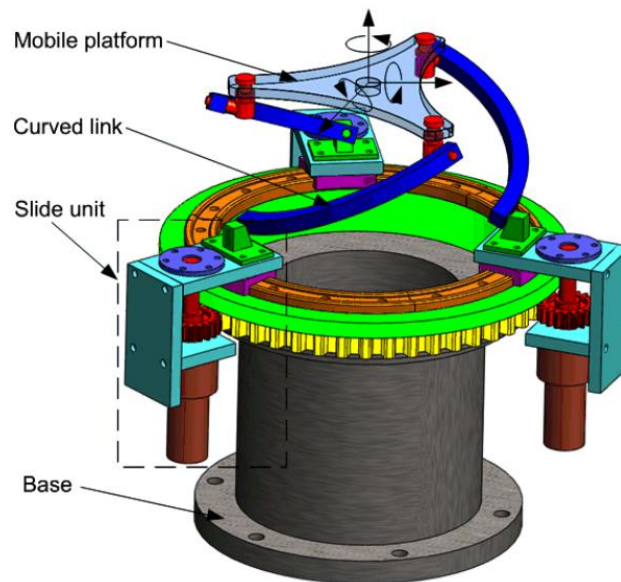
Methods

Figure 3: Reference Design of Candidate SPM [10]

We will be applying the SPM to the end of a common consumer cobot produced by Universal Robots: the UR-10. We will be interfacing with the robot's tool flange, and we want to ensure that all existing tools can still be used with our manipulator. As such, the platform diameter ($d_{platform}$) must accommodate the existing 63mm rotating platform on the UR-10. To ensure easy accommodation of other tooling options we chose a platform diameter of 90mm. The link base diameter (d_{link}) needs to be at least 95mm to clear tool flange, but we cannot have it larger than the tool flange plus an actuator width (~20mm) on each side to keep the design compact. The mechanism height (h) we wanted to bound based on the human wrist. As such, the upper bound is set at 30mm larger than average human metacarpal length and the lower bound is set more compact than a human wrist at the size of reasonable bearings, 10 mm. The angular offset (θ) describes the mounting of the link as seen in Figure 4 below and has its range stem from a variance seen in other literary sources with exploration of SPM's.
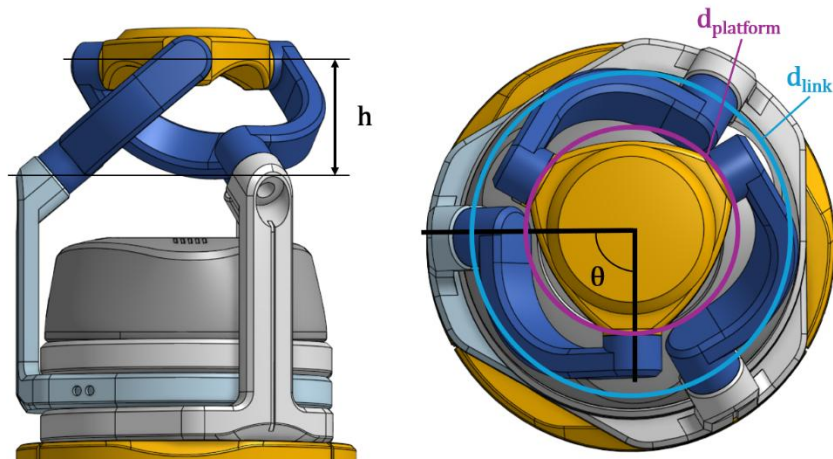

Figure 4. Visual Representation of Four Design Parameters that describe the Kinematic Geometry of the SPM

Beyond the spatial design variables, we want to also consider the mechanical performance of the system under realistic load conditions. As seen in Figure 6 below, the payload capacity of the robotic arm falls off with distance from the robot's center of gravity. A representative use case for the manipulator will be to manipulate a payload positioned directly above the platform freely in the workspace in any orientation. Let's consider we want to handle a 5kg payload that sits up to 100 mm from the platform as our desired load case since this is manipulable across the robot's workspace. This load case causes both a force that deflects the passive linkages and a torque that must be applied by the actuator to maintain the position. Since we aren't concerned with more detailed manipulation tasks for the scope of this evaluation, we will ignore computing torque across various platform positions and loading cases beyond the one described load case. To ensure sufficient overhead to perform dynamic motions, the actuator torque

requirement will be two times the static torque required to hold the payload in place in all orientations. The controller will need to understand the exact torque limitations of the final designed system when manipulating an object in space, but this approximation will get us to a reasonable design selection. Additionally, to achieve accurate end effector positions, the passive links must be stiff under load. Since linkage deflection is not measured by any sensor, the cobot will not be able to accurately account for linkage deflection and will result in inaccurate motion. To address this, we will design the linkage width and thickness such that it deflects less than a prescribed deflection limit of 0.5 millimeters under the load case.
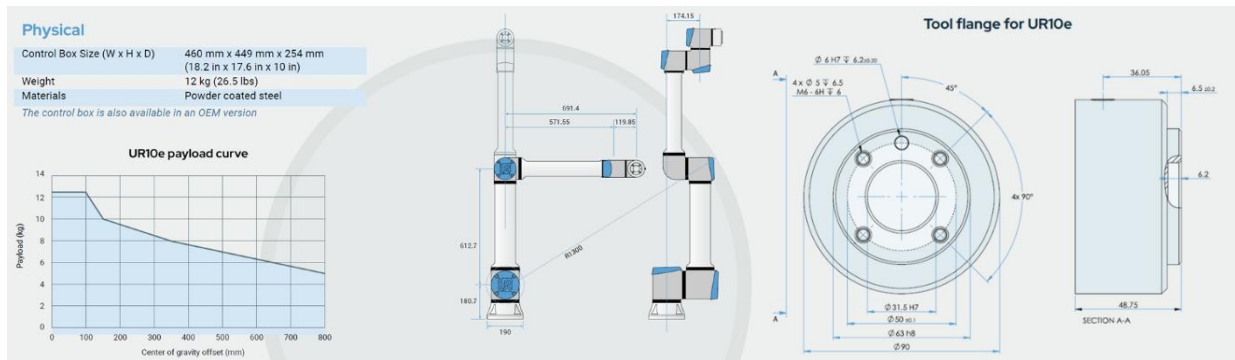

Figure 5. UR-10 Datasheet Parameters

Looking at the design in Figure 3 that we are considering for optimization, the main components that will change with our design variables are the actuator and the linkage. There would be some mass change in the rail that the base of the SPM rides on caused by the base diameter changing; however, the mass change is minor. Thus, we are ignoring its effect in this analysis. Therefore, the mass of the manipulator that changes with our design parameters are due to the mass of the actuator and the mass of the linkage. The sum of three sets of these components represents the mass objective function for the system.

Additionally, we want to ensure that the optimized manipulator allows for a useful range of motion. Height, theta, and the base diameter will help drive this objective. By using GCI, we can effectively evaluate the useful range of motion for a given manipulator.

Having introduced the intention and several constraints behind developing our mechanism, we are choosing to minimize mass and maximize GCI. Optimizing mass allows us to keep a dexterous cobot while also accounting for the impacts of force and torque in the system. Similarly, maximizing GCI ensures that the resulting design is highly manipulable, and useful in giving the cobot added dexterity.

Problem Formulation

Minimize:

Objective 1: Minimize the mass of the system that changes with our design parameters (three actuators and three passive linkages)

Objective 2: Maximize the Global Conditioning Index

$$f_1(\bar{x}) = 3(m_{actuator} + m_{linkage})$$
$$f_2(\bar{x}) = -GCI$$

Subject to:

$$\delta_{linkage} \leq 0.5\text{mm}$$
$$\tau_{actuator} \geq 2\tau_{min}$$
$$10\text{mm} \leq h \leq 100\text{mm}$$
$$30° \leq \theta \leq 150°$$
$$95\text{mm} \leq d_{platform} \leq 125\text{mm}$$
$$d_{link} = 90\text{mm}$$

Simulink Simulation Model

Due to the parallel nature of the manipulator, SPM mechanics are not straightforward to compute with 3D free-body diagrams. Given this, Simulink Simscape Multibody provides an accurate, straightforward, and flexible solution to efficiently understand the mechanics of the system in response to changing inputs and design parameters. We developed a multibody simulation that takes our design parameters, computes the necessary component rotation matrices between the individual bodies, and connects them all together into a model that we can sense forces and torques at all of the joints (see Figure 7).
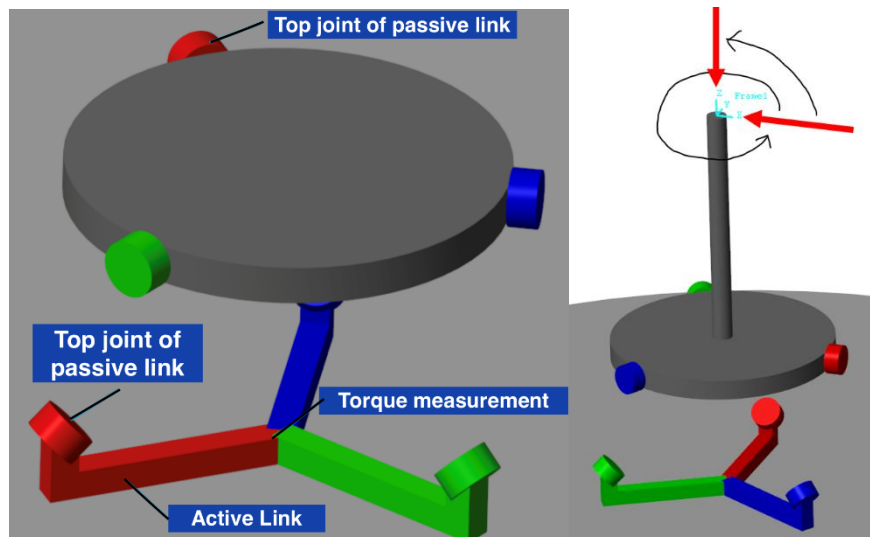
To represent the load case, we are designing around of holding a 5kg object 100mm away from the platform in any orientation in space, a lever arm is added to the platform and a force input is placed on the system. An input force of 50 N is swept around the XY plane before rotating to be directly in line with the Z axis as seen in Figure 6. This load case captures an equivalent load profile as manipulating an object across all orientations. The active link, which represents the carriage that gets driven by the actuator, is commanded to stay in the initial position and a torque sensor is placed on all three of the active links at the labeled measurement position to determine the joint torque an actuator would need to keep the platform from moving throughout the manipulation. A force sensor is placed at the top joint of the passive link to determine the force that would be applied to the linkage causing it to deflect.

Simulink Model Validation

We employed several techniques to validate the force and torque outputs from the Simulink model. The one load case that is easily calculable is the actuator torque needed to resist a torque in the Z axis applied to the lever arm. Since each of the actuators would evenly resist this, the actuators should each require exactly a third of the input torque to maintain position. Running this test case, we confirmed that each actuator torque sensor was equivalent and equal to a third of the input torque. Another method of validation was to compare all of the passive joint sensors across the force sweep. As expected, all of the linkages demonstrated the same force distribution just offset from each other as can be seen in Figure 7. Frome time 0 to 4 seconds, the force is sweeping around the XY plane, then from 4 to 5 seconds, it transitions to directly in line with the Z axis. We can see that at 5 seconds, all of the forces in all of the linkages are equivalent, and that the Z axis of the top joint is 16.67 N, exactly equal to a third of the input force. Similarly, torque goes to zero at this point in time which also makes sense since the force is directly normal to the torque application. These metrics all point to the model being set up and outputting expected values and demonstrate a level of validation sufficient for use in our optimization.
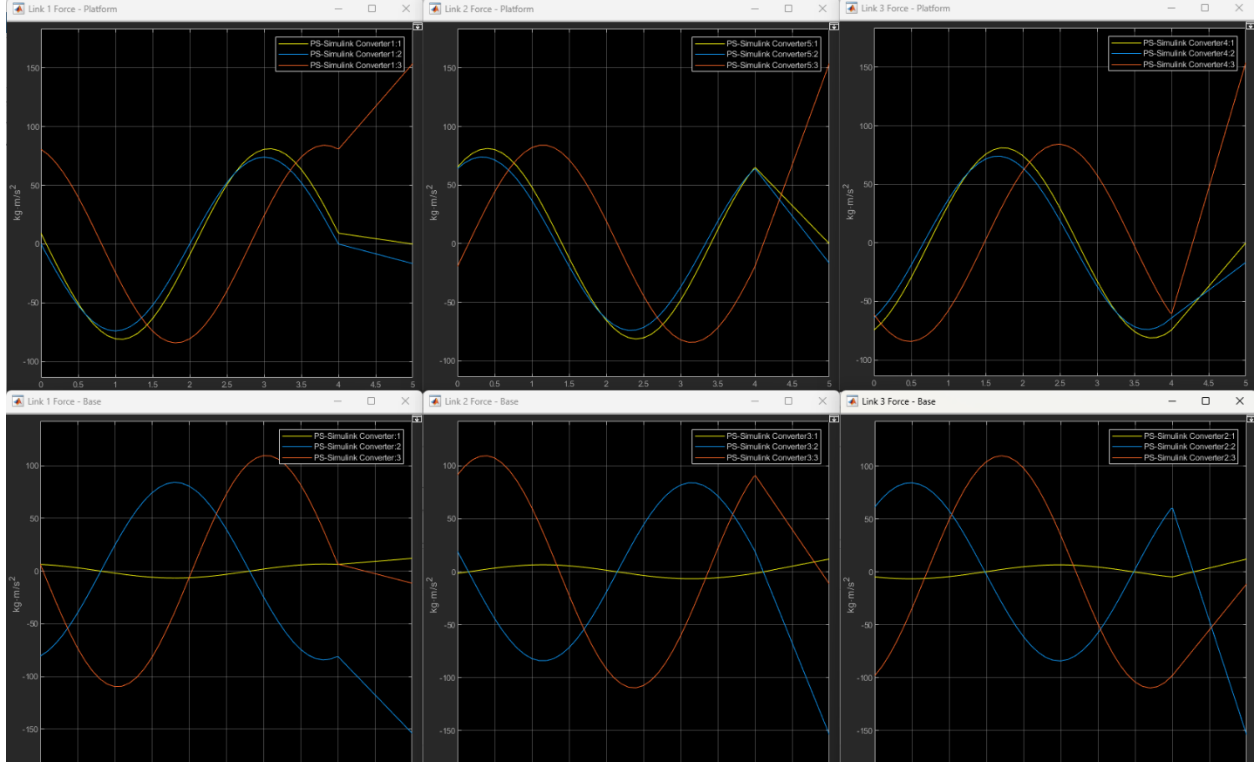
Figure 7. Plots of the XYZ force vectors in the top joint of the passive linkage (top) and the bottom joint of the passive linkage (bottom)
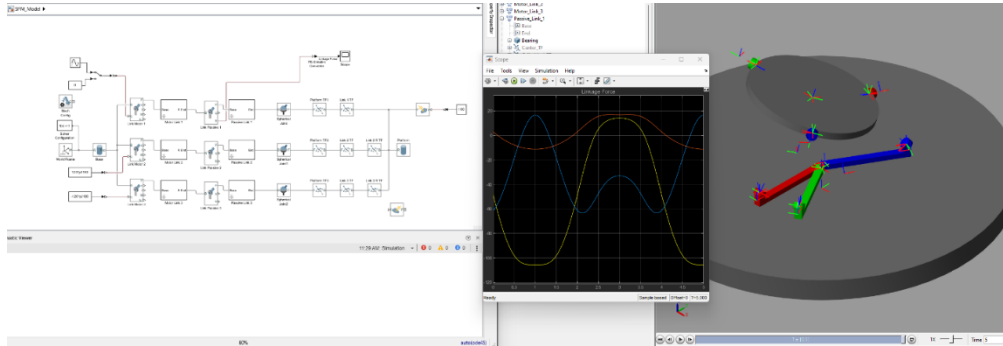

Figure 8. Simulink Model with Torque Output Chart from swinging around one of the joints.

In our system, the dominant sources of mass are the motors and drivetrain components. Since the geometry of the SPM directly affects actuator loading, understanding how different linkage configurations influence joint forces and motor torque requirements is critical to achieving an optimized design. By leveraging the Simscape model, we can extract system-level performance metrics that align more closely with our optimization goals, ensuring that our design decisions lead to improvements in both efficiency and dexterity.

Actuator Selection

To select an appropriate actuator, we need to be sure that the motor has both the appropriate torque and speed for the application. Since our application does not require premium performance, we selected from commercially available off-the-shelf actuators. Additionally, for this application, we have a gear ratio between the motor and the passive linkage. The gear ratio is determined by the ratio of the diameter of the base linkage to the diameter of the gear. We will assume a gear ratio of 6 across all configurations as this reflects gear ratios readily available online at McMaster Carr and simplifies comparative analysis across configurations.

The torque requirement is determined from our Simscape model, which simulates joint loading in the center of the workspace. As previously discussed, we will have a 2x factor of safety (FoS) on the torque to account for dynamic motions. A visual depiction of this can be seen below:

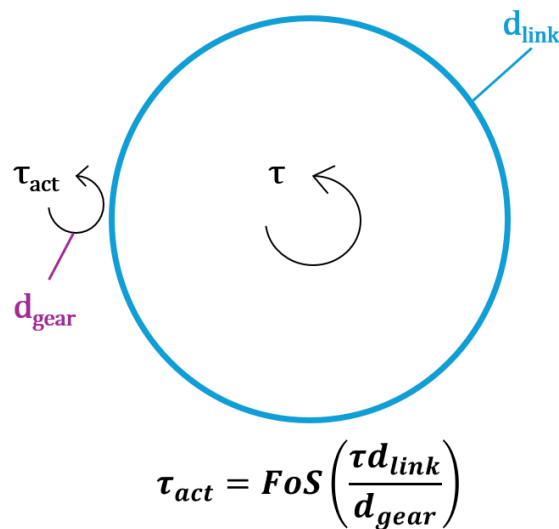$$\tau_{act} = FoS \left(\frac{\tau d_{link}}{d_{gear}} \right)$$

Figure 9: Torque Forces on SPM Model

For responsiveness, we set a minimum actuator speed target: the system should complete a full rotation in under 1.5 seconds, translating to a minimum actuator speed of 240 RPM after accounting for the gear ratio.

We surveyed a broad range of motor types, including brushed DC, brushless DC (BLDC), and stepper motors. Given the torque-speed requirements and space constraints, flat "pancake" BLDC motors emerged as the most promising option. BLDC-servo motors with integrated encoders and closed-loop controllers are ideal for this application, as they reduce system complexity and eliminate the need for external sensors or drivers. While not

all candidates were servo actuators, and no additional weight penalty was applied for non-servo actuators, we might want to prioritize them when performing design tradeoffs. Among the evaluated options, CubeMars motors stood out due to their high torque-to-weight ratio, compact form factor, and cost-effective BLDC-servo options. Their catalog, alongside other comparable motors from multiple vendors, was reviewed, and candidates that met the minimum torque and speed thresholds were compiled in Table 2.

Table 2. Discrete Actuator Options

Part Number	Manufacturer	Motor Type	Rated Torque (Nm)	Max Torque (Nm)	Max Speed (rpm)	Diameter (mm)	Mass (g)	Torque Density (Nm/kg)	Cost
GL30 KV290	CubeMars	BLDC	0.080	0.280	2200	43	41	6.829268293	$ 55.99
GL35 KV100	CubeMars	BLDC	0.150	0.460	815	50	90	5.111111111	$ 54.99
GL40 KV70	CubeMars	BLDC	0.250	0.730	600	46.5	107	6.822429907	$ 91.90
RMD-L-4015 20T	MyActuator	BLDC Servo	0.220	0.490	1010	40	120	4.083333333	$103.00
722-401	Precision Micro Drives	BLDC	0.029	0.252	16380	22	122	2.062622951	$ 88.57
RMD-L-5010 35T	MyActuator	BLDC Servo	0.260	0.650	1015	50	135	4.814814815	$175.45
RO60 KV115-Lite	CubeMars	BLDC	0.800	2.400	5520	60	195	12.30769231	$ 77.90
G006984	iPower Motor	BLDC	0.392	0.392	400	60	207.8	1.887184133	$ 54.44
GL60 KV25	CubeMars	BLDC	0.600	1.750	516	69	230	7.608695652	$136.90
RO60 KV115	CubeMars	BLDC Servo	0.800	2.400	5520	60	248	9.677419355	$ 85.90
R60 KV115	CubeMars	BLDC	0.75	2.3	4150	60	248	9.274193548	$177.90
AKE60-8 KV80	CubeMars	BLDC Servo	5.000	12.500	240	60	260	48.07692308	$272.90
RB-Blu-303	Blue Robotics	BLDC	0.500	0.500	9400	40	282	1.773049645	$160.00
RMD-X4 1:6	MyActuator	BLDC Servo + Gearbox	1.200	1.200	600		300	4	$250.00
36PG-3650BL-14 12V	E-S Motor	BLDC + Gearbox	0.392	0.392	290	36	450	0.871459695	$ 42.50
36PG-3650BL-14 24V	E-S Motor	BLDC + Gearbox	0.784	0.784	570	36	450	1.74291939	$ 42.50
AKE80-8 KV80	CubeMars	BLDC Servo	12.000	30.000	570	80	570	52.63157895	$339.90
DCM4112	Phidgets	BLDC Servo	0.490	0.490	4000	57	4000	0.12254902	$ 83.44

We analyzed how actuator motion maps to end-effector motion for different joint angles. With all joints evenly spaced and sweeping a single joint across various positions, we see joint motion results in changing platform motion in Figure 10. The maximum actuator-to-platform motion ratio was 0.8 and dropped precipitously near the ends of its acceptable joint angles. Although this actuator motion ratio is highly dependent on the joint parameters of the SPM, it highlights how non-intuitive and non-linear the motor output is in the output. Unlike serial manipulators where motion of a single actuator causes linear output motion, SPMs have more complicated motion outside normal operating angles that we are ignoring for this analysis.
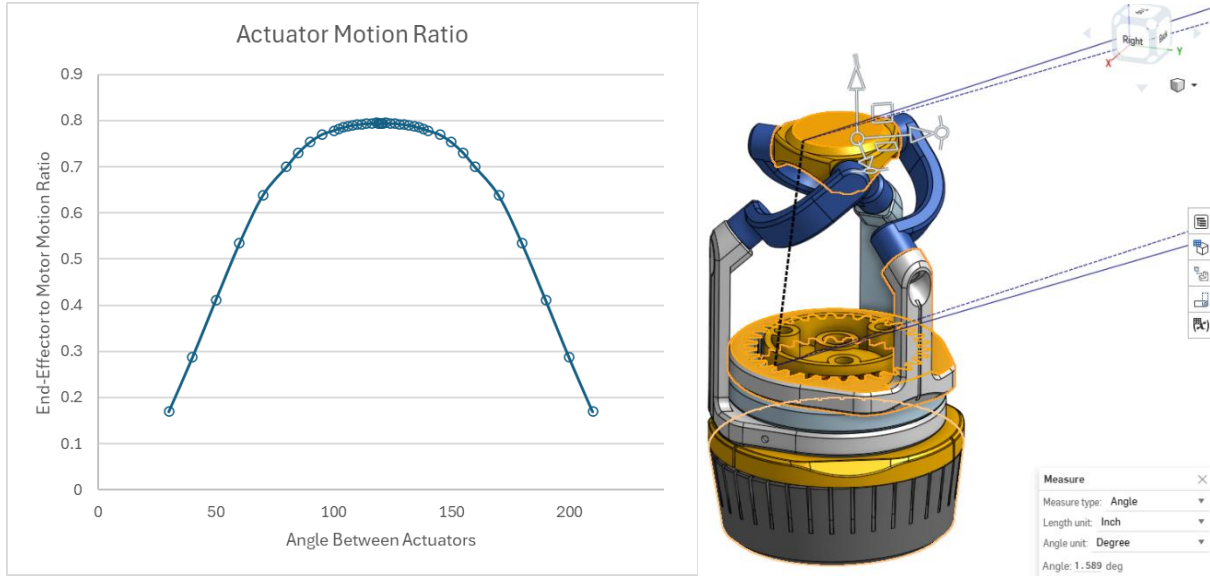
Figure 10: Actuator Motion Ratio (Left) determined for the CAD geometry (Right)

To evaluate each motor's suitability, we developed a MATLAB script that chooses the lightest actuator that satisfies the torque and speed requirements for the given configuration. This will give the most performant motor based on the computed requirements of the configuration.

Structural Model

Finally, we analyze the structural deflection analysis of the linkage beam. These were geometrically modeled as a curved beam defined by the semi-major and semi-minor axes of an ellipse. As seen by the image below:
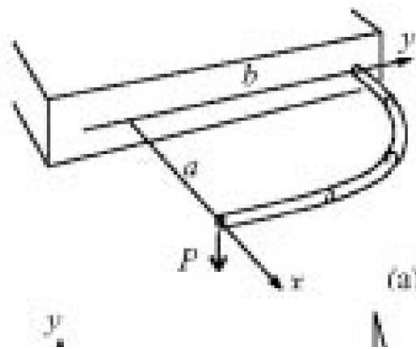

Figure 11: Curved Beam Semi-Major and Semi-Minor Axes

where a load applied as P will produce a moment around the lower pivot point. Given that our NSGA-II algorithm requires thousands of design iterations, the cantilever model's efficiency is crucial. Thus, we took the effective quarter ellipse length and treated that as

12

the length of a cantilevered beam. Then, we used a simple cantilever beam deflection approximation coupled with a gradient descent on the width and thickness. These results were used to find an optimal beam that could resist the applied load from the Simulink with less than 0.5 mm of deflection. The permissible thicknesses ranged from 1.5 mm to 25 mm and widths ranged from 3 mm to 50 mm. The geometric parameters of the curved beam a and b were made functions of the design variables, h and theta, which in turn directly outputted physical design variables a (semi-major axis) and b (semi-minor axis) of the ellipse that represented our model for the curved cantilever beam link as seen the below formula:

The cantilevered beam model uses a quarter-circumference calculation for curved beams, based on the formula:

$$\text{Semi-major axis (a)} = \sqrt{(h^2 + Base\_rad^2)}$$

$$\text{Semi-minor axis (b)} = \frac{Platform\_diam}{2}$$

$$\text{Quarter circumference} = \frac{\pi}{4}\left(3(a + b) - \sqrt{(3a + b)(a + 3b)}\right)$$

The cantilever beam's predicted deflection was then computed by:

$$\text{Cantilever deflection} = \frac{PL^3}{3EI}$$

Structural Model Validation

The cantilevered beam approximation was validated by comparing it as a meta model to predict the deflection of curved beams found in SolidWorks FEA experiments. The experimental beam designs were generated via a Halton sequence of the critical dimensions within their constraints. This resulted in 20 different beam configurations with varying parameters (a, b, w (width), and t (thickness)). Each of these parameters were tested under 4 different loads: 100, 300, 500, and 700 Newtons, giving us a total of 80 test points. The use of the Halton sequence in this experimental design approach was important because it provided good coverage of the parameter space with relatively few test points.
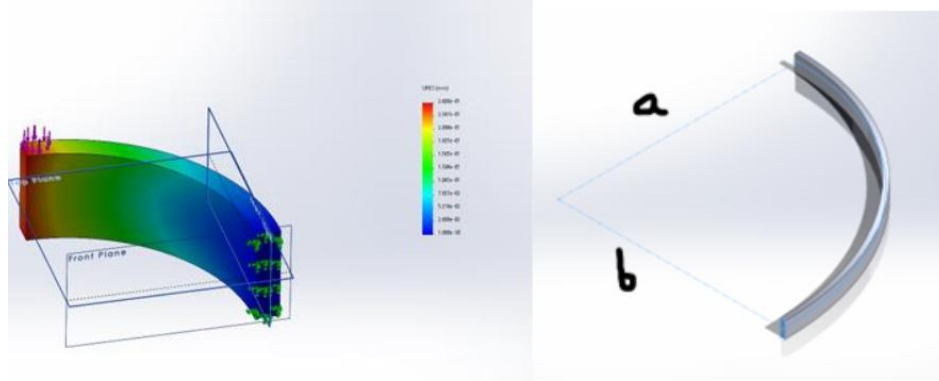
Figure 12: FEA Experimentation Set Up

To properly assess the efficacy of the cantilever beam "meta model" it was tested against two other common meta models that were trained on the generated experimental data. All of these models were then used to predict the experimental data set. This validation used the following models as comparisons to the cantilever beam approximation:

- A Gaussian Process Regression (GPR) model
- A polynomial regression model

The GPR model was trained on the experimental dataset using the MATLAB GPR toolbox. The polynomial model employs a pure quadratic function. Compared to the GPR model, the polynomial model is simpler and did not capture complex nonlinear relationships as effectively. The GPR model was very predictive; however, that broke down when the input deviation strayed too far from the Halton set training data. With respect to both models, the cantilever beam provided a reasonable approximation in a very simple to integrate and reliable manner.

Below are visual plots comparing the cantilever, GPR, and polynomial models, providing an overview of trained data and how predicted vs. actual deflection reacted under loads between 100 N to 700 N. The textured landscape shows many training points clustered together under loads, indicating that the models were similar in deflection under this 3-layered validation process for a physical model. The figure below provides plotted comparison models for beam deflection and their respective errors.
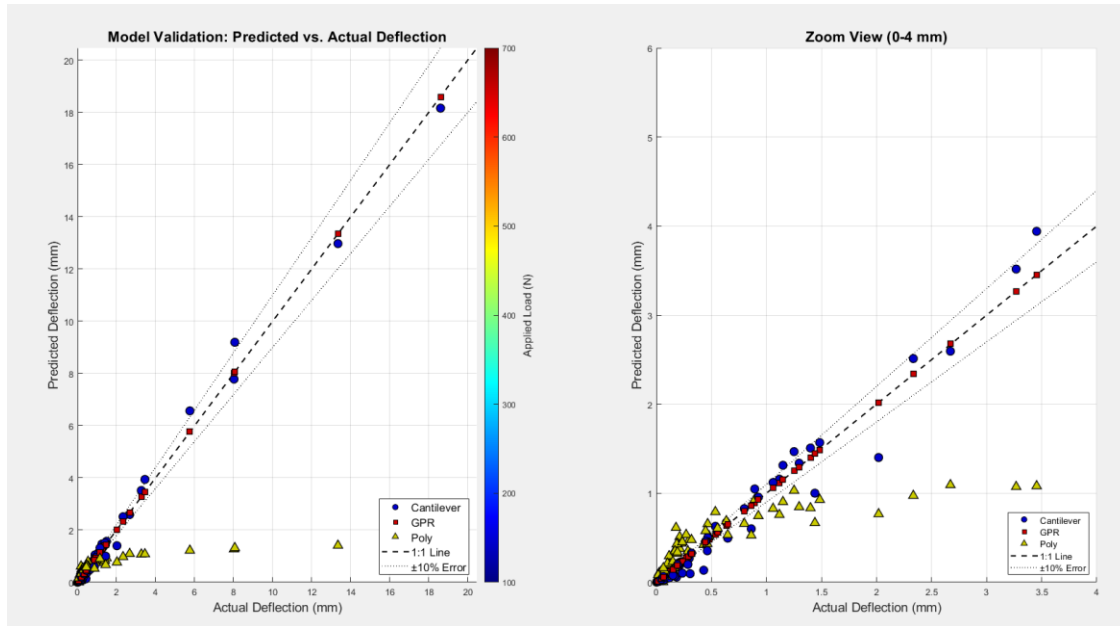
Figure 13: Model Deflection Prediction Error Scatter Plot

Looking over the error it was seen that the predicted deflection was within 10 percent for 12/20 trails conducted. Specifically at the lower bound of loading even with a higher relative deviation effectively the cantilever approximation was slightly conservative by an additional 20% at most. In context that produces a deviation from the actual of at most 2 mm with most other deviations within less than a millimeter.

This overall efficacy of the cantilever approximation is seen in the below histogram where because the cantilever model produces a substantial number of predictions in the low-error bins (0–10%), it supports our decision to use it in the optimization loop—offering computational efficiency without sacrificing acceptable accuracy. Additionally, it's seen that nearly 75% of the cantilever predictions fall within the 20% margin of error which is then compounded that 20% of the deflection limit of 0.5mm is just 0.1 mm or just a 100th of the total height at the lower bound of the mechanism.
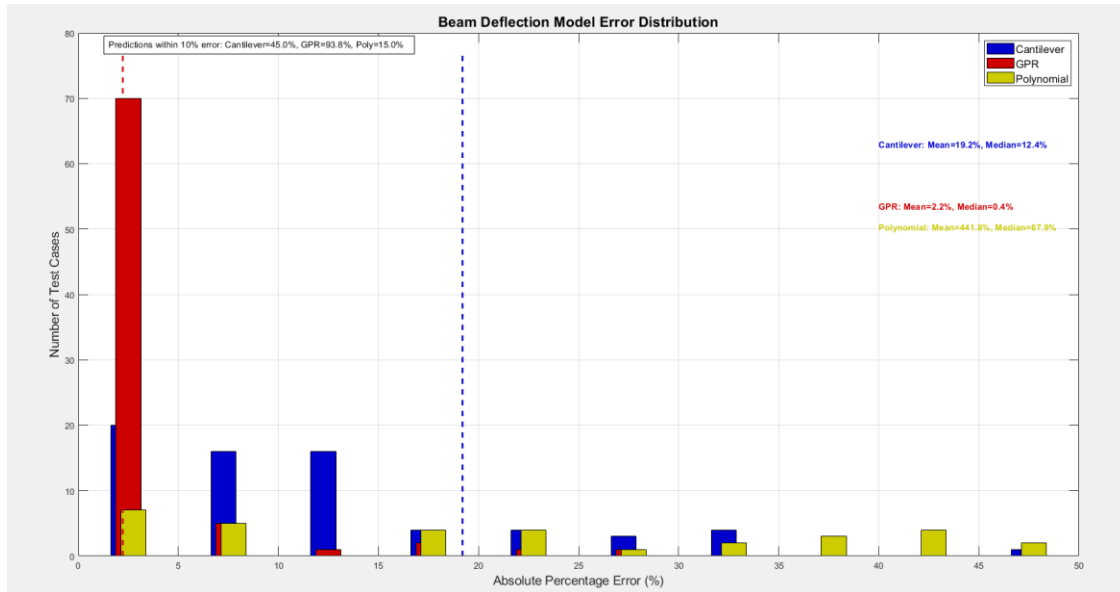
Figure 14: Absolute percentage error between meta models

While certainly the GPR model is extremely predictive it is also extremely dependent on its training dataset so it provides excellent context that something as simple as a cantilever beam approximation could fall under a 20% margin of error. Especially given that this method would be needed in the genetic algorithm, this dependence on training data could have been an inhibiting factor. Given this sensitivity of the GPR models to their training data set if the parameters were ever changed or relaxed larger optimization algorithm would no longer be as predictive. Overall, the cantilever model uses a direct analytical formula which had a faster convergence than the data-driven GPR model. Additionally, unlike the "black box" GPR and polynomial models, the cantilevered beam model has a direct physical interpretation based on classical beam theory making it more interpretable and trustworthy. This validation method then confirmed that the cantilever model maintains reasonable accuracy across the design space.

Kinematics Model

The primary purpose of a kinematic formalization is assessing the range of motion of the SPM, and to justify the choice of the Global Conditioning Index (GCI) as the objective function to assess range of motion. The GCI is a value between 0 and 1 that effectively assesses the manipulator's kinematic dexterity across the workspace it's able to move about. This GCI comes from finding the condition number of the Jacobian matrix defining the manipulator's movement across its workspace and taking the average of the conditioning numbers from all the swept orientations evaluated at each point of movement. A GCI that is closer to 1 implies a manipulator is precise and the motion of the manipulator is controlled. Having the GCI be one of our objective functions will give an idea of how closely the SPM comes to performing like a human wrist in terms of wrist rotation.
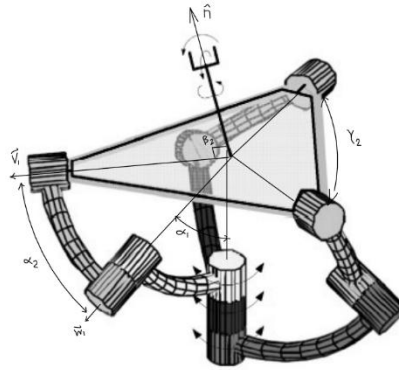

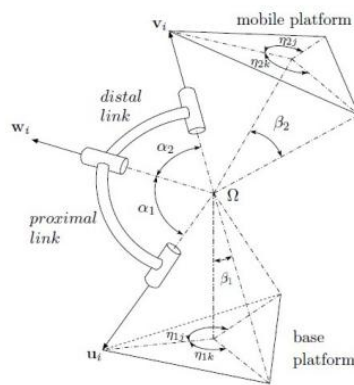*Figure 15: Kinematic Model of Spherical Parallel Manipulator with Additional Notation*

Figure 16: Generic Spherical Parallel Manipulator geometry with respect to the ith link

The figures above depict some of the primary angles that influence the kinematics of the coaxial SPM as well as the vectors on the axes that run through the joints of the SPM. The

joints are represented as cylinder shapes at the ends of the distal and proximal links. Below is a table of the variables that go into the kinematics function to output a GCI.

Table 3: Kinematic Design Variables

Variable	Variable Type	Description
α_1 (deg)	Continuous (determined by H, θ, base diameter)	Angle made by vectors $\mathbf{V}_i$ and $\mathbf{W}_i$*
α_2 (deg)	Continuous (determined by H,θ, α_1, SPM radii of platforms)	Angle made by vectors $\mathbf{U}_i$ and $\mathbf{W}_i$*
β_2 (deg)	Discrete	Angle kept at 90°
η_{11} (deg)	Discrete	Angle kept at 0°
η_{12} (deg)	Discrete	Angle kept at 120°
η_{13} (deg)	Discrete	Angle kept at 240°
γ_2 (deg)	Discrete	Angle between vectors $\mathbf{V}_i$, angle is kept at 120°*
H (height in mm)	Continuous	Primary design variable, height of the SPM
θ (deg)	Continuous	Primary design variable, angle made by vectors $\mathbf{V}_i$ and $\mathbf{W}_i$ projected onto the mobile platform's plane*
D (diameter in mm)	Continuous	Primary design variable, diameter of base platform

*"i" represents which linkage the variable is being attained, Total Linkages: 3

The variables above are utilized to determine the vectors $\mathbf{V}_i$ and $\mathbf{W}_i$ using forward kinematics and inverse kinematics. Once these vectors are calculated, a Jacobian matrix is made from the set of $\mathbf{V}_i$ and $\mathbf{W}_i$, and this matrix is used form the GCI for each instance of theta that our system aims to iterate through. The following equations were used to determine the vectors $\mathbf{V}_i$ and $\mathbf{W}_i$:

$$w_i = \begin{bmatrix} \cos{(\eta_{1i} - \theta_i')}\sin{\alpha_1} \\ \sin{(\eta_{1i} - \theta_i')}\sin{\alpha_1} \\ -\cos{\alpha_1} \end{bmatrix}$$

$$v_i = Qv_{0i}$$

$$v_{0i} = \begin{bmatrix} -\sin{\gamma_2}\sin{\beta_2} \\ \cos{\gamma_2}\sin{\beta_2} \\ -\cos{\beta_2} \end{bmatrix}$$

In the equations above, Q is a rotational matrix around the axes of the mobile platform. The angles that make up this rotational matrix are z,Ψ, and Φ. They are represented in Figure 16. θ_i' is the angle the ith linkage rotates about the unit vector $\mathbf{u}_i$. To generate the workspace of any manipulator via inverse kinematics a discretized range of Euler angle orientations are given for which inverse kinematics will deterministically solve for the input angles theta1, theta2, and theta3 that reach that orientation. Each orientation for a given "pose" will have its Jacobian matrix determined as previously described and then its inverse

condition number evaluated. Below is a workspace with various orientations reach and with "singular" configurations note in red where the inverse condition number was near 0.
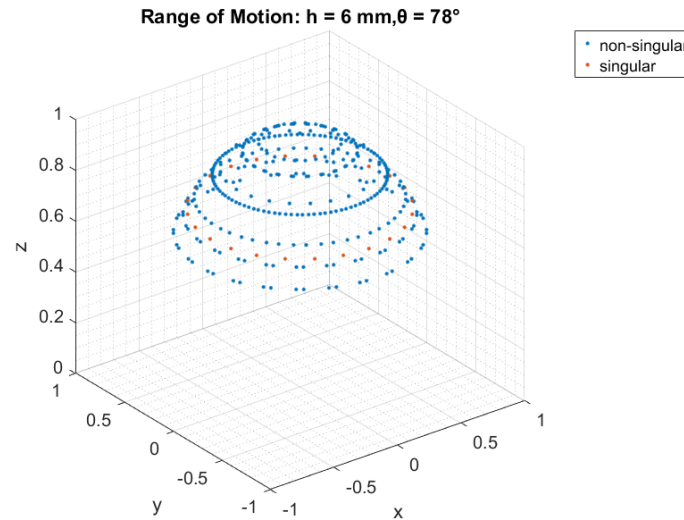

Figure 17. Workspace data set for Coaxial SPM

Now each point in this workspace can be evaluated for this condition number and that would similarly show a "heat-map" variation that helps visualized what a well-conditioned workspace for the SPM looks like:
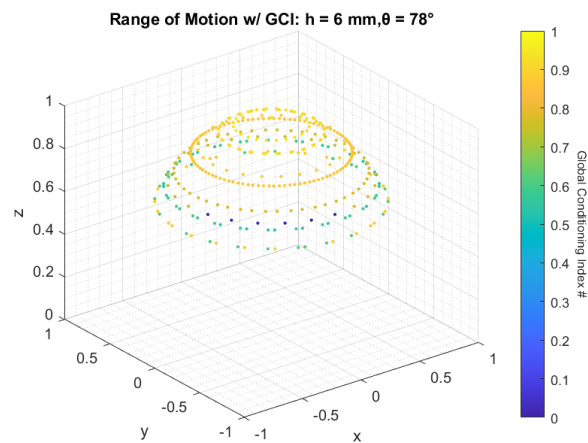

Figure 18. Workspace data set for Coaxial SPM

Finally, by averaging all the inverse condition numbers for the orientations seen in the workspace as a quality metric the global conditioning index can be determined.

Kinematics Validation

To ensure the kinematic calculations are correct and consistent with previous research, we compare the position calculated from our formalization with a physical model in Mier's "Design of a Spherical Parallel Robotic Wrist Mechanism". Specifically, we compared the vectors V_i shown in Figures 15 & 16. In Mier's paper, he positions the SPM prototype such that the joint between the proximal and distal linkages and the joint between the distal link and mobile platform make an angle μ_i where "i" represents the linkage it's taken from. These joints can be seen in Figure 16. This angle is made on the X-Y plane as if looking down onto the SPM from above. Mier sets their physical prototype to the angles of 100°, 50°, and 80° to get the following vectors:

$$v_1 = [-0.8722, \ -0.2643, \ 0.4116]$$

$$v_2 = [0.5684, \ -0.6876, \ -0.4519]$$

$$v_3 = [0.3038, 0.9519, 0.0400]$$

Implementing the same angle into our kinematic workspace yields the following vectors:

$$v_1 = [-0.872394, \ -0.263939, \ 0.411419]$$

$$v_2 = [0.568053, \ -0.687760, \ -0.451997]$$

$$v_3 = [0.303978, 0.951843, 0.039903]$$

Calculating the relative average error of each vector and averaging, we obtain a percent error of 0.07% between Mier's physical prototype and our kinematic formulation. This demonstrates the accuracy of our calculations for our SPM.

In addition, to ensure our kinematics are consistent with our SPM model and demonstrate the feasibility of the model to translate to the positions calculated, we orient the model at a point determined by the edge of our constraints on the system. We apply a height of 0.1 m, a base diameter of 0.125 m, and a theta of 150° to get the following set of orientations:
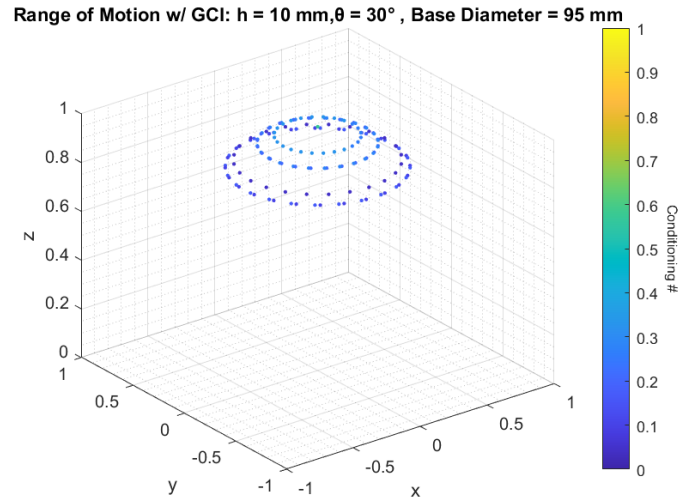
Figure 19. Workspace data set for Edge-Case Implementation

With the set of points generated, we translate the Simscape model to a point representing the furthest point of movement the SPM can achieve (i.e. the outside points of the dome in Figure 19). Doing so gives us the following model:
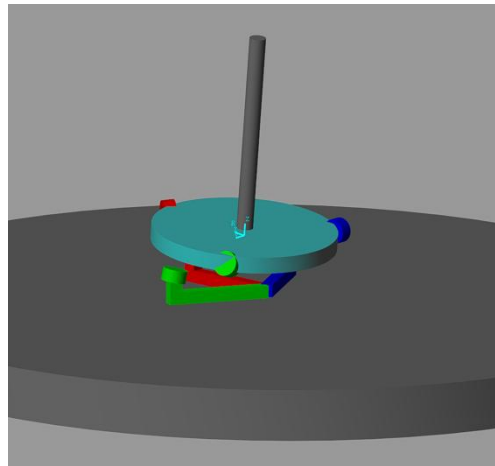

Figure 20. SPM Model Representation of Edge-Case Workspace

Figure 20 shows that the edge-case kinematic solutions we calculate are feasible and can be applied to a physical representation of the SPM.

NSGA-II Optimization Architecture

The combined outputs—linkage mass, actuator mass, and kinematic performance—feed directly into our objective functions. The NSGA-II algorithm then evaluates these objectives (minimizing total mass while maximizing global conditioning index) and generates new design candidates for the next iteration utilizing a probability of crossover of 90% and mutation probability of 33.3%. This creates a continuous optimization loop that converges toward the Pareto frontier of optimal designs.

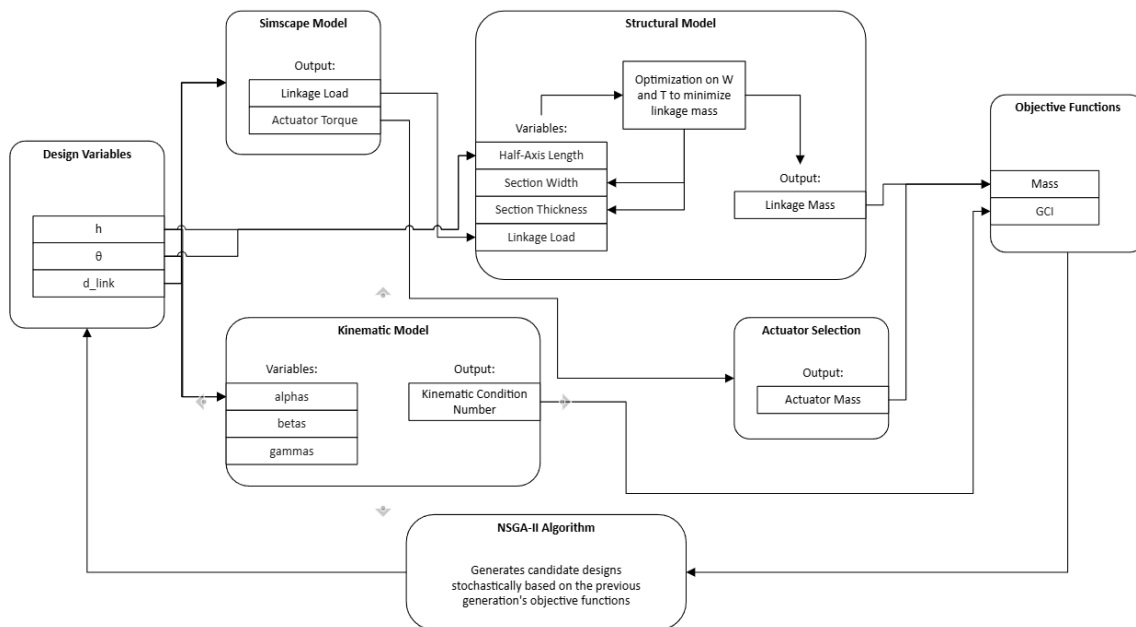Below provides a flow chart depicting the algorithm looping process as summarized above:

Figure 21. SPM Optimization Flowchart

For each candidate design in the genetic algorithm, our system follows the workflow shown in Figure 21. Starting with the design variables (height, angle θ, and base diameter), we first generate a Simscape multibody simulation to determine the linkage loads and actuator torque requirements. Based on the actuator torque, our selection module identifies the lightest motor that satisfies the torque and speed requirements. Simultaneously, the structural model determines the optimal link dimensions (width and thickness) that minimize mass while meeting deflection constraints under the calculated linkage loads. The model employs an interior-point gradient-based optimization algorithm to find the optimal cross-sectional dimensions that minimize mass while meeting structural requirements. The mass from both components is combined to form our first objective function.

If a viable linkage configuration is found that satisfies the structural constraints, the kinematic model generates the workspace using forward and inverse kinematics and calculates the global conditioning index (GCI). This forms our second objective function. When a design fails to meet deflection criteria, a significant penalty is applied to both objective functions to ensure it doesn't progress in the optimization.

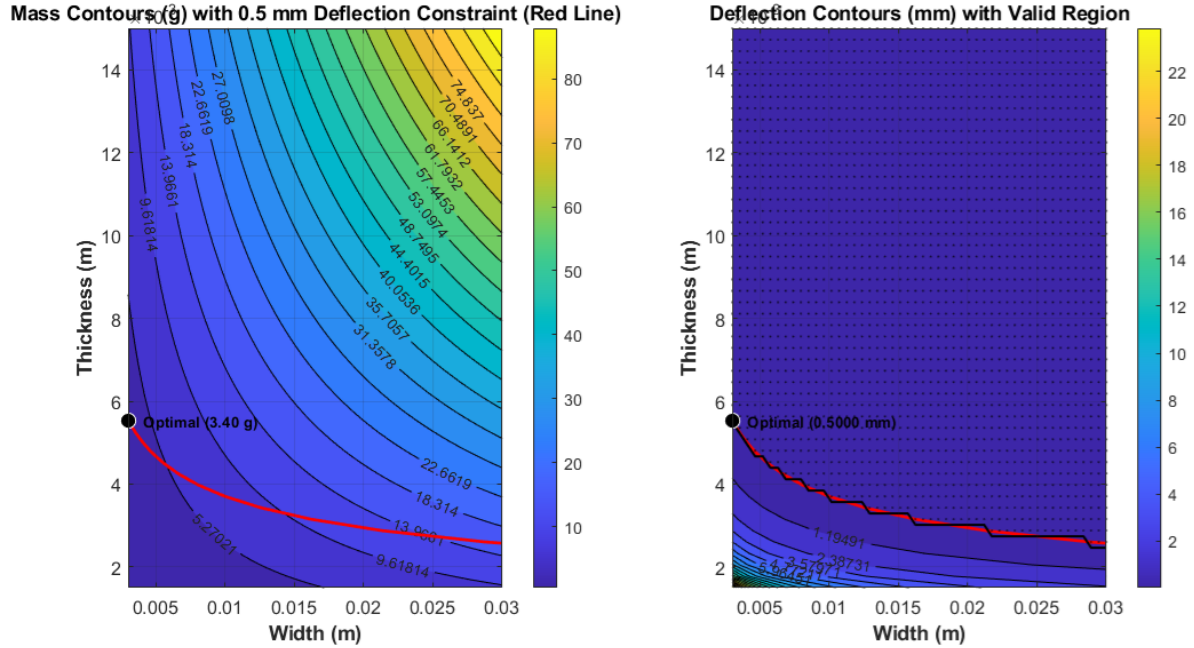*Figure 22. Cross-Dimensional Affects on Mass Surrogate*

Figure 23. Beam Optimization with Deflection constraint for a Sample set of Design Parameters (Left) Mass contours (g) with the 0.5 mm Deflection Constraint shown as a red line (Right)

Results

Multi-Modal Objective Landscape

To supplement the NSGA-II optimization, we used a Halton sequence to conduct a low-discrepancy sampling of the design space. This technique allowed us to visualize how individual parameters influenced system performance without stochastic issues resulting from the genetic algorithm. The results exposed a strongly modal relationship between the objective functions and the design variables. For instance, torque and force requirements varied dramatically with small shifts in linkage position, revealing tight performance bands separated by areas of poor performance. Similarly, GCI exhibited sharp peaks within narrow regions of the parameter space, indicating that dexterity optimization is highly sensitive to configuration details.
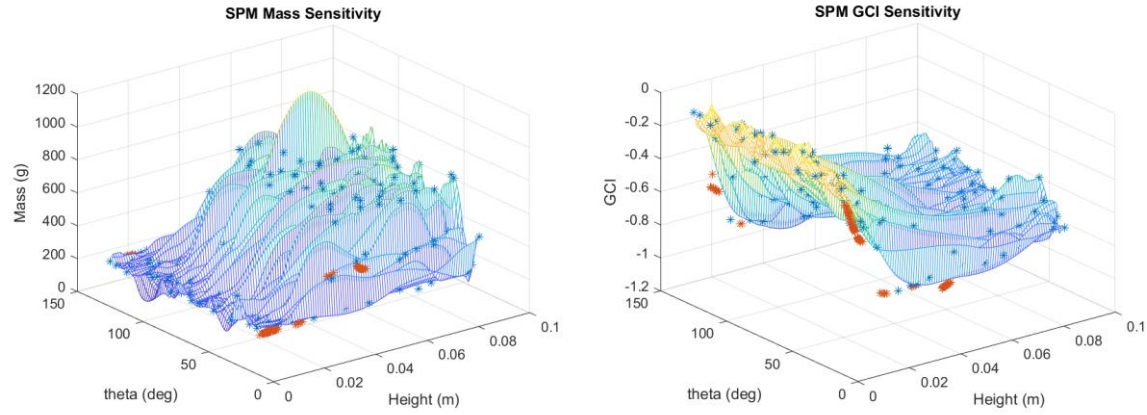
Figure 24. SPM Halton design space exploration (blue) overlaid with the 80/30 NSGA-II solution (orange)
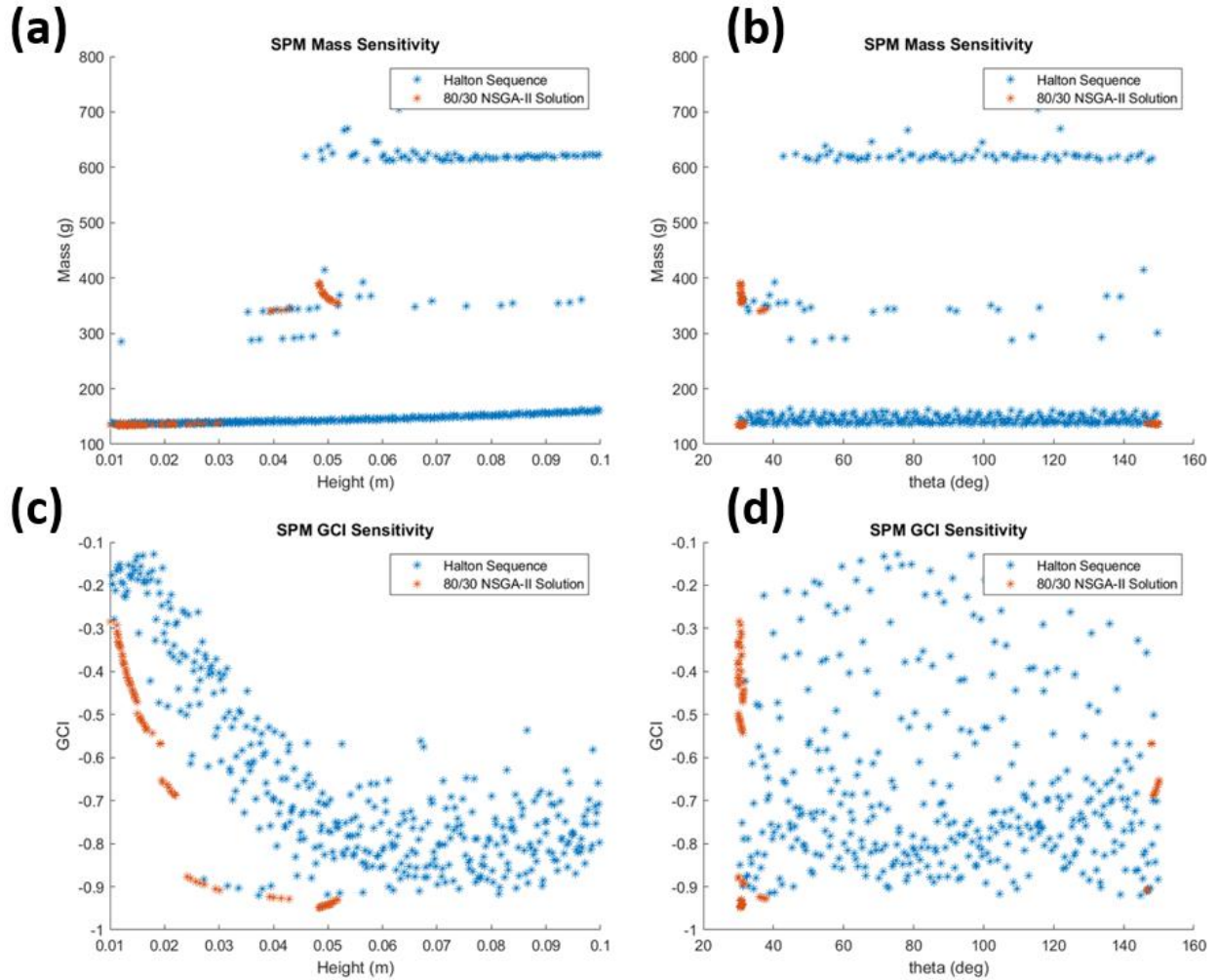

Figure 25. SPM Halton and 80/30 NSGA-II solutions plotted with h and theta plotted against mass and GCI. Sensitivity to platform diameter was not significant as it was almost always at the minimum value.

Comparing the NSGA-II results, the 80/30 Pareto front reveals distinct clusters at approximately 135g, 150g, and 350-390g of mass, matching the steep transitions visible in the mass sensitivity Halton plot. These clusters directly correspond to discontinuities in the surface where actuator selection changes occur. The GCI sensitivity Halton plot confirms that the best GCI values occur at lower heights and higher theta values, which aligns with the location of the lightweight (~135g) Pareto solutions. The thorough design space exploration run provides comprehensive coverage of these transition boundaries, with optimal solutions strategically positioned at the performance "cliffs" visible in both Halton surfaces. In comparison, the 40/10 Pareto front captures the same essential clusters at 130-140g and ~600g, though with fewer intermediate solutions. When compared to its corresponding Halton plots, we observe that these Pareto solutions correctly identify the same critical transition boundaries visible in the 80/30 case, particularly the steep mass gradient at higher heights. The 40/10 run successfully locates solutions at the optimal GCI region (lower height, higher theta) while also finding the high-performance GCI points at higher mass values, demonstrating that even with reduced computational effort, the optimization effectively identifies the key design trade-offs visualized in the Halton surface plots.

These patterns highlight the complexity of the design space and reinforce the selection of the NSGA-II algorithm to navigate the landscape. Unlike gradient-based methods that would get trapped in local minima, NSGA-II was able to discover distinct families of solutions distributed across a complex performance landscape. For example, two solutions with nearly identical mass and torque outputs could yield vastly different GCIs due to subtle differences in linkage attachment height and angle. The algorithm's ability to maintain diversity across the population proved essential for capturing the full range of high-performing designs.

Trial Runs

The following trial runs were conducted for the NSGA-II runs: population 20/generation 5, population 40/generation 10, population 40/generation 20, and population 80/generation 30. This strategic selection of population and generation combinations allowed us to evaluate how population size affects solution diversity and determine the minimum generations needed for convergence. This approach allowed us to understand computational efficiency by efficient NSGA-II population and generation sizes for the SPM design problem that balanced computational cost against optimization quality.
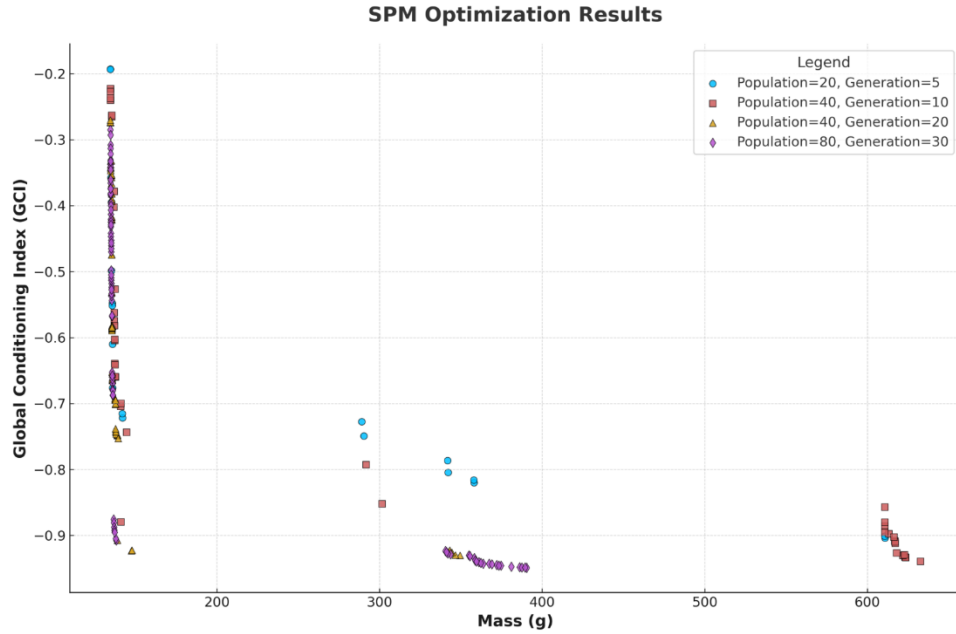
Figure 26. Pareto Fronts of All Optimization Trials

Figure 26 above depicts the various rank 1 solutions determined by the NSGA-II algorithm for the different trial runs we conducted. From this, we can identify three distinct clusters of data at masses less than 200 g, masses between 250 g and 400 g, and masses greater than 600 g. These clusters of data represent the actuator selection by the NSGA-II algorithm. From this, we see the lightest actuator identified is able to satisfy the constraints for this first cluster and achieves a large spread of GCI values. Since heavier actuators are only selected by the algorithm when it achieves higher GCI values, we only see designs selected with high GCI values. Additionally, the existence of those solutions indicates that the heavier actuators are able to achieve higher manipulability than the solutions with the lightest actuator.
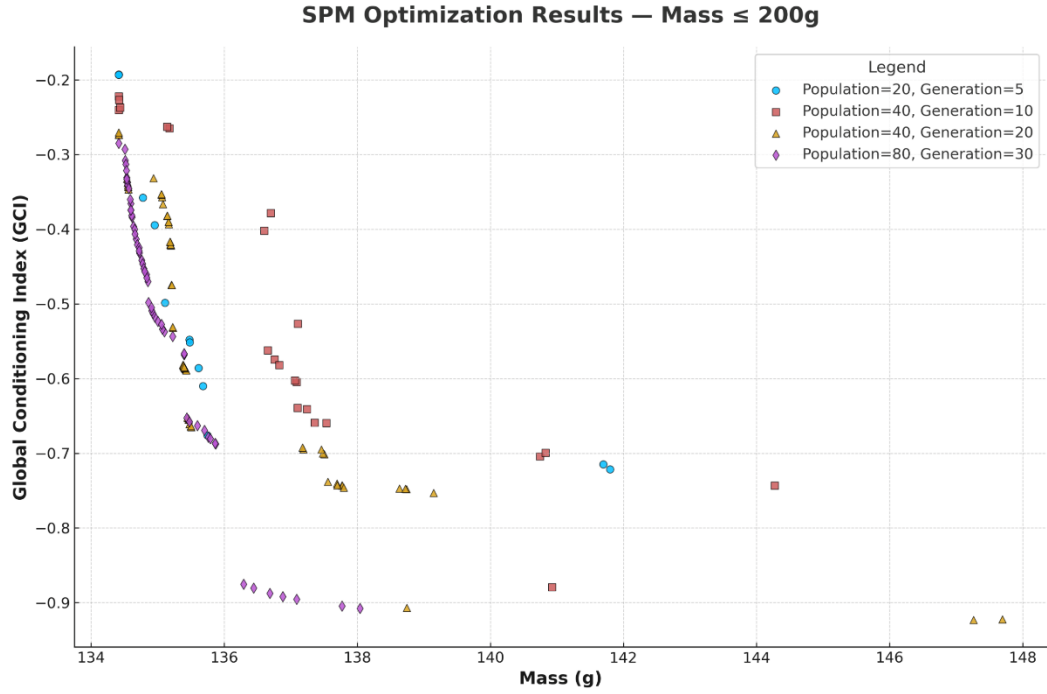
Figure 27. Optimal Solutions of All Trial Runs at Most Optimal Actuator

Figure 27 not only demonstrates the performance of the optimization at different populations and generations, but it also depicts clearly the pareto front created by a population of 80 and generation count of 30. Utilizing the solutions generated from each set of data, we utilized compromise programming to determine the optimal solution for each dataset. The equation below shows the formula used in compromise programming where Z represents the optimum, W_i represents the weights applied to objective functions, f represents the objective function, f_i represents the target value, and p was selected as 2 to represent the Euclidean distance. The target value was set as the minimum value within each dataset.

$$Z = \left\{ \sum_{i=1}^{q} \left(\frac{W_i(f_i(\bar{x}) - f_i^*)}{f_i^{\max}} \right)^P \right\}^{1/P}$$

Table 4. Optimal Solutions for each Dataset

Dataset (Population/Generation)	Height (m)	Θ (°)	Base Diameter (m)	Mass (g)	GCI

20/5	0.06107	89.33	0.095353	610.896	0.903914
40/10	0.06154	148.28	0.111072	623.330	0.933156
40/20	0.04592	39.37	0.102171	349.381	0.930075
80/30	0.03011	146.69	0.096016	138.040	0.907728

It is clear from Table 4 that a population of 80 and generation count offers the most optimal solution amongst our datasets. It provides anywhere from a 153-352% decrease in mass when compared to the other results. The difference in GCI is negligible as it only differs by 0.4-2.8% across the different datasets. The figure below depicts where this optimal solution lies.
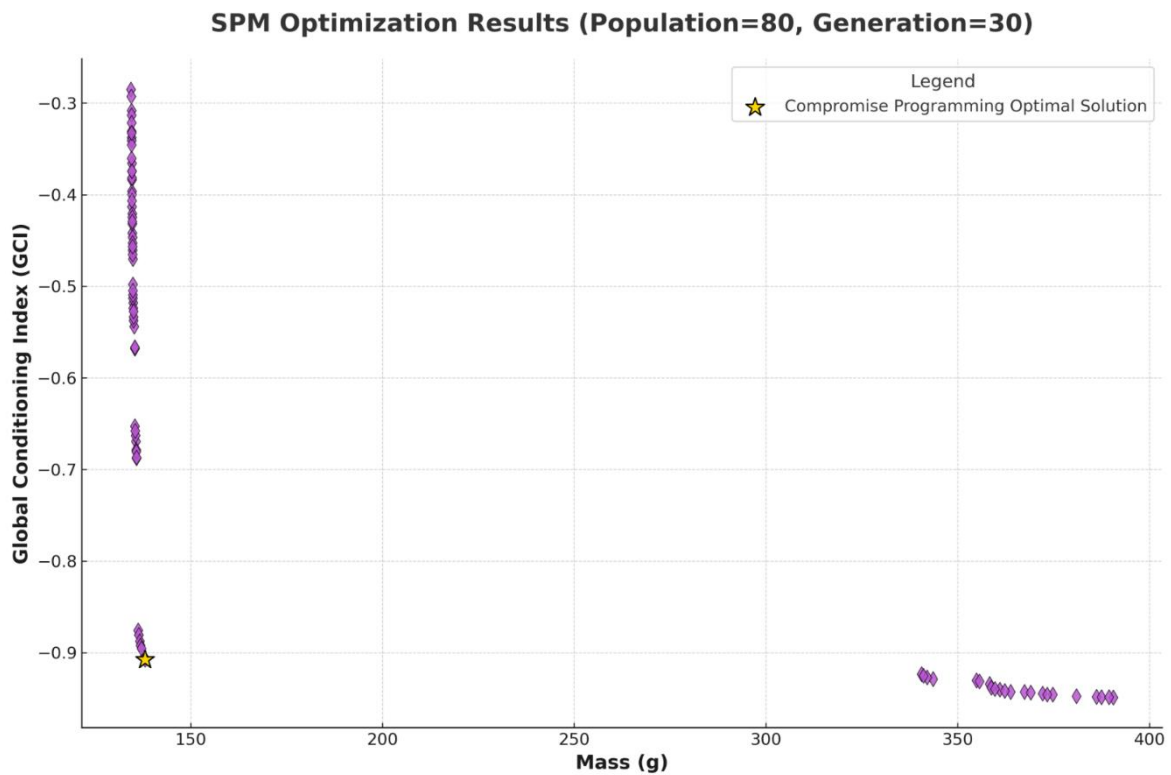

Figure 28. Optimal Solution for Population of 80 and Generation of 30

The kinematic workspace generated from this optimal solution can be seen below.
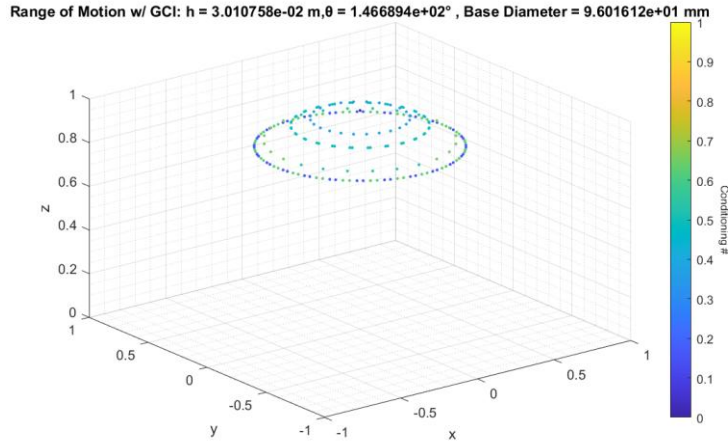
Figure 29. Optimal Solution Kinematic Workspace

Figure 29 details the conditioning numbers associated with each orientation kinematics was conducted for, and it gives a normalized view of the movement the optimal SPM can achieve with the minimization of mass and maximization of GCI.

Discussion

Based on using compromised programming for a population of 80 over 30 generations, the optimal design balancing minimal mass and maximal GCI is the SPM model described by the table below and visualized as seen in Figure 30. The chosen actuator of this system was the GL30 KV290, which was the lightest option and one of the most torque dense. The finalized linkage dimensions were 3 mm wide, 10 mm thick, axis a and b dimensions of 45mm and 56.6 mm. This produced a beam with a weight of 6.46 grams which was within 0.02 grams of the true weight reported by SolidWorks.

Table 5. Optimal Solution

Optimal Solution				
GCI	Mass (grams)	Height (mm)	Theta (deg)	Base Diameter (m)
0.91	138	30	146.7	96
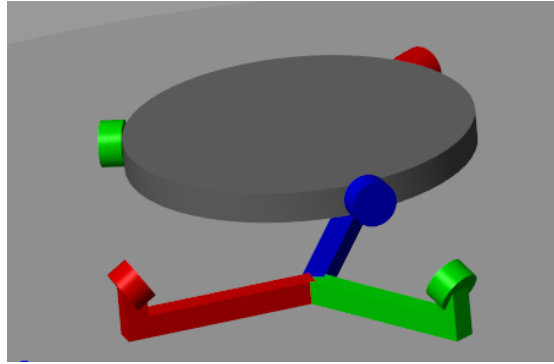
Figure 30: Visual depiction of the SPM with our optimal design parameters.

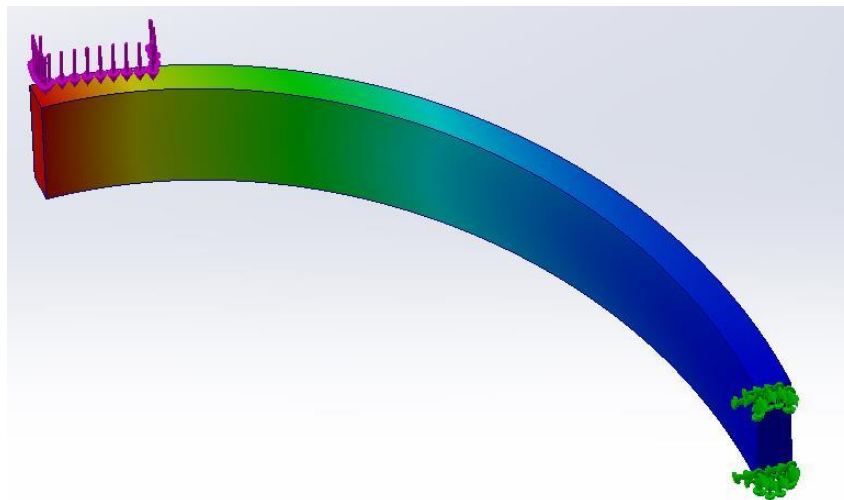*Figure 31: The chosen actuator of the Optimal Solution: GL30 KV290*

Figure 32: The optimized linkage for the SPM

The multi-objective optimization revealed several important trends and tradeoffs in the design of the SPM. Using the NSGA-II algorithm, we explored a wide range of feasible solutions in our optimization for mass and GCI. The clear Pareto Frontier observed across

many different stochastic runs of the optimization algorithm demonstrates the inherent trade-off between mass and dexterity in the mechanism.

One of the most significant observations was the discontinuity in the Pareto frontier. This discontinuity is directly attributable to the use of discrete motor options. Because actuator mass is a non-continuous variable tied to commercially available units with fixed torque and speed characteristics, there are several locations where changes in dexterity require switching to a larger, heavier actuator. As a result, if we are confident in our torque overhead, we would opt for a solution just before a discontinuity to maximize GCI for a given actuator. Conversely, if we desired a higher torque overhead, we would choose a solution further away from the discontinuity.

Further analysis of the design space revealed that configurations achieving higher GCIs generally required greater joint torques and more robust linkages to transmit these loads. While load impacts on the system mass are less pronounced than selecting a heavier actuator, there is still an increase in mass due to stiffer linkages needed to handle the deflection forces. This trend reflects the physical coupling between stiffness and dexterity: increasing the range and uniformity of motion across the workspace inherently exposes the structure to less favorable load paths and higher moment arms. To accommodate this, optimized solutions skewed toward larger passive linkages with increased cross-sectional dimensions, which in turn added to the system's overall mass. These findings reinforce the importance of including both structural and dynamic performance in the optimization formulation.

Additionally, one prior assumption was that the kinematic performance would be largely influenced by the height of the manipulator, however that was not necessarily the case. With there being a reasonable spread of performance for varied heights as seen in Figure 25c.

Two critical assumptions were regarding self-collisions and linkage deflection. The elimination of self-collisions allowed us to simplify the kinematic workspace analysis and not require more refined tools such as robotic simulators like Gazebo. The other was our modelling of linkage deflection could have allowed excessively stiff solutions. By coupling this with a gradient descent to find a width and thickness to minimize mass we effectively found permissible configuration in this scenario and delineated some of this risk.

Through the process of testing with the optimization we also experimented with removing the base diameter variance and by changing the bounds to see what sort of effects occurred. Typically we had seen that the optimization via the genetic algorithm still pooled based on the discrete variables but the remove of the base diameter variance negatively

impacted finding better kinematic configurations. With this as an added variable, we were able to more thoroughly explore possible solutions.

Overall, the multi-tiered, complex model developed here creates a physically meaningful model for exploration of the solution space. Initially, we believed including kinematic parameters to be too computationally expensive and analytically challenging. However, their integration served to be incredibly useful in informing our solution space. This impact was evident in the final design set, where high-performing solutions demonstrated orientation sweeps comparable to a human wrist when tested in Simulink. Another added complexity that richly informed the design space was the inclusion of discrete actuators. The computed torque loads drove the NSGA-II algorithm to generally fall into pools of solutions separated by actuators. Since the actuator's mass accounted for nearly 75% of the system mass, this added complexity really expanded the detail in the design space. Effectively, this showed that for a given actuator the physical parameters of the SPM could be configured to be mass optimal with an excellent GCI. For the defined load case, the optimization correctly prioritized solutions within the lighter actuator pool. These configurations offered strong kinematic performance with lower overall mass, aligning well with our multi-objective criteria.

Conclusion:

Overall, some of our key-takeaways were around properly scoping and approaching a large-scale optimization problem. We chose a very complex engineering task to analyze, and upon much discussion and reflection as a team, were able to make appropriate simplifications to sufficiently answer the problem within a reasonable scope for the class. During this endeavor, we struggled with leveraging new toolboxes and methods to rapidly iterate, assess, and refine solutions. We learned the value of distilling the problem down to its most critical and basic form to create a solid foundation for further analysis. Techniques like genetic algorithms, which once seemed intimidating, became approachable through a strong grasp of the fundamentals from class, and became increasingly demystified through application in this project. Some challenges arose in developing functional models for dynamic, kinematic, or structural systems, which proved to be the crux of the complexity at times. For example, crafting a fast, reasonably accurate proxy for deflection showed the trial-and-error process needed to simplify complexity while maintaining utility within the broader optimization. We also found it insightful to study how geometric parameters influenced kinematic performance and how load distribution across SPM linkages and actuators followed non-intuitive patterns. These findings helped us better understand the interplay between design geometry and

performance outcomes. Overall, the project reinforced how critical model fidelity and thoughtful system decomposition are to meaningful optimization. Specific to the spherical parallel manipulator, this project served as an excellent entry point to gain a deeper understanding of parallel robot mechanisms.

Future Prospects

We presented a set of models and an initial structure to generate an optimized SPM based on methods explored in class. While a majority of time was spent on setting up and running the optimization presented, future work could be done to better address specific structural or torque requirements. Specifically, to torque, our narrowly scoped load case was developed to efficiently answer design requirements that varied throughout the feasible region, but a more rigorous analysis could include multiple load cases at a variety of manipulator poses to really understand the capabilities of the manipulator. The developed Simulink model can be extended to assess how specific poses, load cases, and motion paths impact required torque and force loads within the system. This was avoided initially due to model instability throughout various joint angles across the design space, but once a more narrowed set of designs were identified, a more detailed analysis could be conducted on additional load cases.

Furthermore, the identified solution could have a more detailed design run to both confirm the solution and further optimize the linkage. A physical prototype of the system could be generated to confirm the design space is adequately addressed in the optimum design (e.g. rigidity and manipulator motion). Additional optimization of individual components could be done with the identified design parameters. For example, additional optimization could also be done on the passive linkages such as topology optimization to generate a more mass efficient beam geometry than the simple rectangular beam solved for here

Lastly other objective functions could be introduced to further provide options for optimization such as the inclusion of gearing or other kinematic parameters such as manipulability. Such items would effectively help create an even higher fidelity optimization model which would serve the start of physical prototyping very well by having even more of its parameters defined and optimized for.

If we were to revisit the project, we would explore neural networks and other metamodeling techniques more deeply, potentially decomposing the SPM into independently modeled subsystems. One of the key limitations in our current optimization was the approximately 20 second evaluation time per simulation which constrained the number of designs we could evaluate. By training surrogate models or neural networks on

subsystem behaviors, we could drastically reduce computation time and enable more efficient exploration of the design space. This approach would be especially well-suited for handling discrete design choices, where we noticed our applied optimization methods struggled.

References

1. Jaworski, Łukasz, & Karpiński, R. (2017). BIOMECHANICS OF THE HUMAN HAND. *Journal of Technology and Exploitation in Mechanical Engineering*, *3*(1), 28–33. https://doi.org/10.35784/jteme.536

2. Vaisman L, Dipietro L, Krebs HI. A comparative analysis of speed profile models for wrist pointing movements. IEEE Trans Neural Syst Rehabil Eng. 2013 Sep;21(5):756-66. doi: 10.1109/TNSRE.2012.2231943. Epub 2012 Dec 10. PMID: 23232435; PMCID: PMC4689593.

3. Pitzalis, R.F.; Park, D.; Caldwell, D.G.; Berselli, G.; Ortiz, J. State of the Art in Wearable Wrist Exoskeletons Part I: Background Needs and Design Requirements. Machines 2023, 11, 458. https://doi.org10.3390/ machines11040458

4. J. Tian, C. Li, C. Li, G. Li, D. Zhou and Z. Ju, "Improving Wrist Angle Recognition Accuracy under Different Load Conditions," 2019 IEEE 9th Annual International Conference on CYBER Technology in Automation, Control, and Intelligent Systems (CYBER), Suzhou, China, 2019, pp. 1267-1272, doi: 10.1109/CYBER46603.2019.9066741. keywords: {Wrist;Muscles;Fatigue;Electromyography;Neural networks;Feature extraction;Eigenvalues and eigenfunctions},

5. Cornelius, Cory & Sorber, Jacob & Peterson, Ronald & Skinner, Joe & Halter, Ryan & Kotz, David. (2012). Who wears me? Bioimpedance as a passive biometric.

6. Mahmoud Elsamanty, et al. "Workspace Analysis and Path Planning of a Novel Robot Configuration with a 9-DOF Serial-Parallel Hybrid Manipulator (SPHM)." *Applied Sciences*, vol. 13, no. 4, 6 Feb. 2023, pp. 2088–2088, https://doi.org/10.3390/app13042088.

7. Patel, Vatsal V., and Aaron M. Dollar. "Robot Hand Based on a Spherical Parallel Mechanism for Within-Hand Rotations about a Fixed Point." *IEEE Xplore*, 1 Sept. 2021, ieeexplore.ieee.org/stamp/stamp.jsp?tp=&arnumber=9636704. Accessed 5 Nov. 2022.

8. Swann Schilling. "3D-Printed Harmonic Gearbox Robot Arm." *YouTube*, 18 Jan. 2025, www.youtube.com/watch?v=hrzzEMh_b4I. Accessed 28 Apr. 2025.

9. Sephien, Andrew, et al. "Inter-Relationships of Metacarpals 1 to 5, Regarding Their Length, Metaphyseal Midshaft Width, Articular Surface Area of Head and Base, Age, and Sex: A Cadaveric Study." *HAND*, vol. 16, no. 5, 28 Oct. 2019, pp. 706–713, https://doi.org/10.1177/1558944719880026. Accessed 19 Feb. 2024.

10. Wu, Guanglei. "Ultiobjective Optimum Design of a 3-RRR Spherical Parallel Manipulator with Kinematic and Dynamic Dexterities." *Modeling, Identification and Control: A Norwegian Research Bulletin*, vol. 33, no. 3, 2012, pp. 111–121, https://doi.org/10.4173/mic.2012.3.3. Accessed 10 Feb. 2022.